Mechanics and Mechanical Engineering
Vol. 21, No. 3 (2017) 611–635
© Lodz University of Technology

CFD Simulation of Heat Transfer and Fluid Flow within Metallic Foam in Forced Convection Environment

Salim Boulahrouz
Department of Mechanical Engineering
Abbes Laghrour University
Khenchela, 40000, Algeria
boulahrouz_salim@yahoo.fr

Yvan Avenas
University Grenoble Alpes
G2Elab, F-38000 Grenoble, France
yvan.avenas@g2elab.grenoble-inp.fr

A. Chehhat
Department of Mechanical Engineering
Abbes Laghrour University
Khenchela, 40000, Algeria
LESEI Laboratory, Faculty of Engineering
University of Batna
05000, Algeria
achehhat@gmail.com

Received (25 March 2017)
Revised (16 June 2017)
Accepted (21 July 2017)

In the present study, a CFD simulation of forced convection in a rectangular block of aluminum foam is investigated. A two energy equations model with the Brinkman-Forchheimer extended Darcy model is considered in the CFD investigation. The governing equations are solved using COMSOL, a commercial multiphysics finite-element PDE solver. Three types of aluminum foam 10-, 20-, 40- pore per inch with different porosity are studied. A parametric study for the range of Reynolds number Re = 250–2000 and the imposed heat flux $q_w = 0.8 - 1.6$ (W/cm^2) is carried out to examine the thermal and the fluid flow behaviors of the aluminum foams. It is found that the plug flow conditions are prevalence for the aluminum foams. The 40-pore per inch aluminum foam has a better heat transfer performance with a larger pressure drop, followed by the 20-, and then by the 10- pore per inch. The validation of the simulation results is made against experimental data from the literature and showed a perfect agreement.

Keywords: aluminum foam, CFD modeling, COMSOL, cooling, Darcy–Brinkman–Forchheimer model, forced convection.

1. Introduction

The use of open-cell metal foams have been widely increasing given by its diverse properties in various areas including aerospace, electronics and automotive. These cellular materials are considered one of the most promising enhanced surfaces by virtue of their intrinsic multifunctional features: high heat transfer area to volume ratio, good stiffness and strength, enhanced flow mixing capability. Therefore, metal foams have considerable possible applications in heat exchangers [1], fuel cells [2], metal foam reactors [3], solar air receivers [4], compact heat sinks for power electronics [5, 6]. Metallic foams are used for other important industrial applications such as: cladding on buildings, strain isolation, geothermal operations, petroleum reservoirs, cryogenics, catalytic beds, compact heat exchangers for airborne equipment, air-cooled condensers for air conditioning and refrigeration systems [7, 8].

Several investigations on the determination of the heat transfer and fluid flow characteristics of metallic foam have been conducted over the last twenty years. Bhattacharya et al. [9] provided analytical and experimental results for the effective thermal conductivity for high porosity metal foams. They used a range of high porosity materials of $90 < \varepsilon < 98\%$ and 5, 10, 20 and 40 PPI pore densities. The analytical model represented the foam by a two-dimensional array of hexagonal cells. The porosity and the pore density were used to describe the porous media. Experimental data with aluminum foams using air and water as the fluid media were used to validate the analytical solutions. Their experimental work also made use of the Forchheimer equation to describe the flow parameters. Phanikumar and Mahajan [10] numerically and experimentally studied the buoyancy induced flow in a high porosity aluminum foam heated from below and indicated the two-equation energy model is a better model when fluid/porous interfaces are involved. Haji-Sheikh and Vafai [11] provided analysis of heat transfer in porous media imbedded inside ducts of different shapes, by solving the governing equations assuming local thermal equilibrium, and applying a constant-wall-temperature boundary condition. Alvarez–Hernandez [12] and Dukhan [13] presented experimental results for the pressure drop of airflow through samples of open cell aluminum foam for various porosities and pore densities. Minkowycz and Haji-Sheikh [14] solved the local-thermal-equilibrium equations for the case of parallel plates and circular porous passages including the effect of axial conduction. Kopanidis et al. [15] presented a 3D numerical simulation methodology for the flow and heat transfer at the pore scale level of high porosity open cell metal foam. The conjugate flow and temperature fields were obtained by solution of the Navier–Stokes and energy equations for two different foam pore densities under various flow and temperature conditions. Chen et al. [16] presented a numerical investigation for enhanced heat transfer from multiple discrete heated sources in a horizontal channel by metal-foam porous layer. Both Darcy–Brinkman Forchheimer flow model and two-equation energy model based on local thermal non-equilibrium were used to characterize the thermo-flow fields inside the porous regions. A stream function–vorticity analysis solution was used to resolve the coupled governing equations for the porous/fluid composite system. Bai and Chung [17] developed a simplified analytical model and a unit-cell CFD model to predict the heat transfer capability and the pressure drop in metal foams. Dukhan and Ali [18] presented results of a systematic experimental study targeting the effect of foam sample diameter and wall effects on the viscous and form contributions to the pressure drop for air flow through aluminum foam. Ranut et al. [19] presented a 3D approach based on the X-ray computed microtomography (μ-CT) technique. The results were performed on three different open-cell aluminum foams samples and showed that open-cell aluminum foams are effective means for enhancing heat transfer.

In this work, a two energy equations model coupled with the Brinkman-Forchheimer extended Darcy model are solved by the commercial CFD software "COMSOL". The computational domain consists of a rectangular block of open cell aluminum foam. This porous medium is heated by its above surface with uniform and constant heat flux and exposed to ambient air flow. The effects of Reynolds number range Re = 250-2000 and the imposed heat flux $q_w = 0.8 - 1.6$ W/cm^2 on the fluid flow hydrodynamic parameters, as well as on the porous medium thermal characteristics are examined to establish the fundamental effects, and provide a practical results.

2. Thermo-fluid model

We consider a rectangular block of open-cell aluminum foam having a constant cross section and heated by its top surface with a constant and uniform heat flux q_w. The block has a length L in the flow direction and a height H, as shown in Fig. 1. One-dimensional flow of air is considered in the x direction. At the inlet of the foam block, the air flow has a constant average velocity u_0 and a temperature T_0.

2.1. *Assumptions*

1. Flow through porous media involves three scales: The pore scale, the representative elementary volume (REV) and the domain scale. The REV is much larger than the pore scale, but smaller than the domain scale. The REV is the length scale at which the characteristics of porous flow hold [20]. For the purposes of this work, transport properties (heat, mass and momentum) are considered to have averaged-volume values at the REV and system models are generated from this scale.

2. Thermophysical properties of both solid and fluid phases are constant; this assumption is valid in applications where the temperature is not sufficiently high to cause changes in the properties of the materials.

3. Foam porosity is constant and independent of the management. The porous medium is isotropic and homogeneous [21]. There are no significant variations with the direction for a given foam type.

4. At the flow speed considered, the flow is steady, laminar and incompressible.

5. Radiative heat transfer, viscous dissipation and the work done by pressure changes are negligible.

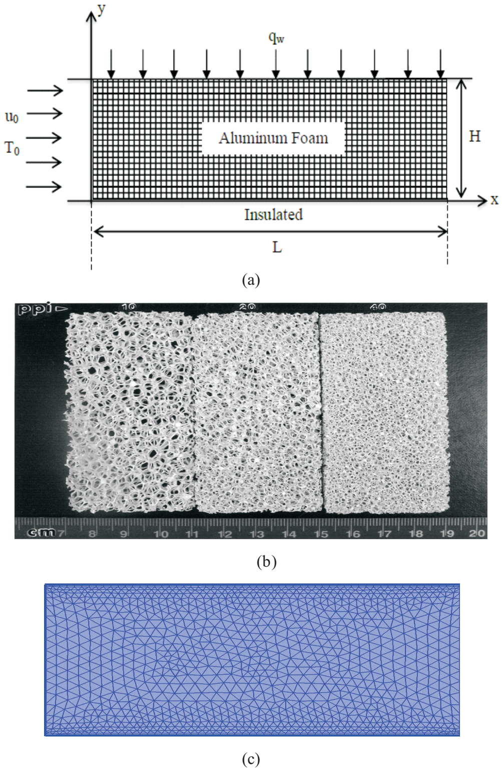

Figure 1 a) Schematic of foam block subjected to a constant heat flux, b) Samples of different pore density aluminum foam with a graduated millimeter scale [40], and c) Mesh grid system for the computational domain

2.2. *Governing equations*

Under the assumptions above, the two dimensional steady state macroscopic conservation equations for mass, momentum and energy of solid and fluid phases are as follows [38]:

- Continuity equation:

$$\frac{\partial u}{\partial x}+\frac{\partial v}{\partial y}=0 \tag{1}$$

  Assuming the air is incompressible at the flow speed considered.

- Momentum equations:

  x-momentum equation:

$$\frac{\rho_f}{\varepsilon^2}(u\frac{\partial u}{\partial x}+v\frac{\partial u}{\partial y})=-\frac{\partial p}{\partial x}-\frac{\mu u}{K}-\frac{\rho_f C_F}{\sqrt{K}}\left|\overrightarrow{V}\right|u+\frac{\mu}{\varepsilon}(\frac{\partial^2 u}{\partial x^2}+\frac{\partial^2 u}{\partial y^2}) \tag{2}$$

y-momentum equation:

$$\frac{\rho_f}{\varepsilon^2}(u\frac{\partial v}{\partial x}+v\frac{\partial v}{\partial y})=-\frac{\partial p}{\partial y}-\frac{\mu v}{K}-\frac{\rho_f C_F}{\sqrt{K}}\left|\overrightarrow{V}\right|v+\frac{\mu}{\varepsilon}(\frac{\partial^2 v}{\partial x^2}+\frac{\partial^2 v}{\partial y^2}) \tag{3}$$

- Energy conservation equations: Energy conservation equation for the fluid phase:

$$(\rho C_p)_f\,(u\frac{\partial T_f}{\partial x}+v\frac{\partial T_f}{\partial y})=\frac{\partial}{\partial x}((k_{fe}+k_d)\,\frac{\partial T_f}{\partial x})+\frac{\partial}{\partial y}((k_{fe}+k_d)\,\frac{\partial T_f}{\partial y}) \tag{4}$$
$$+h_{sf}a_{sf}\,(T_s-T_f)$$

Energy conservation equation for the solid phase:

$$0=\frac{\partial}{\partial x}(k_{se}\frac{\partial T_s}{\partial x})+\frac{\partial}{\partial y}(k_{se}\frac{\partial T_s}{\partial y})+h_{sf}a_{sf}\,(T_f-T_s) \tag{5}$$

The dimensionless parameters used in the present study are:

$$X=\frac{x}{H}\qquad Y=\frac{y}{H} \tag{6}$$

$$\mathrm{Re}\;=\frac{\rho_{\mathrm{f}}u_i H}{\mu} \tag{7}$$

$$Nu_x=\frac{h_{sf}H}{k_f}=\frac{q_w H}{(T_{wx}-T_i)\,k_f} \tag{8}$$

Calmidi [21, 22] developed a model for d_f/d_p as a function of porosity after modification to reflect the difference between the open cell represent and the three-dimensional dodecahdron structure. The fiber diameter, d_f, is measured by using a microscope. The pore diameter d_p is estimated by counting the number of pores in a given length of material.

$$\frac{d_f}{d_p}=1.18\sqrt{\frac{(1-\varepsilon)}{3\pi}\frac{1}{G}},\quad G=1-e^{-\frac{(1-\varepsilon)}{0.04}}\ \text{(shape function)} \tag{9}$$

The properties of porous matrix of metal foam, K and C_F, for momentum equation are taken from Calmidi [22] as follows:

$$C_F=0.00212\,(1-\varepsilon)^{-0.132}\left(\frac{d_f}{d_p}\right)^{-1.63} \tag{10}$$

$$\frac{K}{d_p^2}=0.00073\,(1-\varepsilon)^{-0.224}\left(\frac{d_f}{d_p}\right)^{-1.11} \tag{11}$$

The thermal properties of metal foam, k_{fe}, k_{se}, k_d and α_{sf}, for energy equation are taken from the literature [23–26] and are shown as follows:

$$k_{eff}=k_{fe}+k_{se}=\varepsilon k_f+B\,(1-\varepsilon)^{0.763}\,k_s,\ \ \mathrm{B}=0.181\text{ for air} \tag{12}$$

$$k_d=\gamma\rho C_p\sqrt{K}\left|\overrightarrow{V}\right|,\ \text{where }\gamma=0.06\ \text{(the dispersion coefficient) for air} \tag{13}$$

$$a_{sf}=\frac{3\pi d_f}{(0.59d_p)^2}\left[1-e^{-(1-\varepsilon)/0.04}\right] \tag{14}$$

2.3. *Boundary conditions*

The following boundary conditions are imposed on the model above. All conditions at the limits are physically significant:

At the inlet (x = 0, 0 ≤ y ≤ H), the flow with input velocity is given.

$$u = u_0 \qquad v = 0 \qquad T_f = T_0 \qquad \frac{\partial \mathrm{T_s}}{\partial x} = 0 \tag{15}$$

At the exit (x = L, 0 ≤ y ≤ H), atmospheric pressure and no viscous stress.

$$p = p_0 \qquad \mu\left(\nabla \mathrm{u} + (\nabla \mathrm{u})^T\right) = 0 \tag{16}$$

Along the bottom wall (0 ≤ x ≤ L, y = 0), the no-slip conditions are taken.

$$u = 0 \qquad v = 0 \tag{17}$$

Without heat sources:

$$\frac{\partial T_f}{\partial x} = 0 \qquad \frac{\partial T_s}{\partial x} = 0 \tag{18}$$

Along the top wall (0 ≤ x ≤ L, y = H), the no-slip conditions.

$$u = 0 \qquad v = 0 \tag{19}$$

With heat source:

$$q_w = -k_s \frac{\partial \mathrm{T_s}}{\partial \mathrm{y}} \Big|_{\mathrm{y=H}} - \; k_f \frac{\partial \mathrm{T_f}}{\partial \mathrm{y}} \Big|_{\mathrm{y=H}} \tag{20}$$

Where L = 5.08 cm and H = 10.16 cm.

In this study, we use three types of aluminum foam, whose properties are given in Table 1.

Table 1 Properties of the three types of aluminum foam [20]

ppi (pore-per-inch)	ε (%)	σ ($\mathrm{m^2m^{-3}}$)	k_{se} ($\mathrm{Wm^{-1}K^{-1}}$)	d_p (m)
10	68.6	1264	27.0	$1.84\mathrm{x}10^{-3}$
20	78.2	1705	21.3	$2.03\mathrm{x}10^{-3}$
40	93.5	1915	18.7	$1.20\ \mathrm{x}10^{-3}$

3. Results and discussion

The aluminum-foams made of aluminum-alloy T-6201, are employed in the present study. The density and thermal conductivity are almost identical for the aluminum-alloy, i.e. ρ_s = 2690 $\mathrm{kgm^{-3}}$ and k_s = 218 $\mathrm{Wm^{-1}\ K^{-1}}$. Air is used as the working fluid (Pr = 0.7, ρ_f = 1.16 $\mathrm{kgm^{-3}}$ and k_f = 0.0263 $\mathrm{Wm^{-1}K^{-1}}$) [16].

For aluminum foam cooled by air, the temperature of the solid and the fluid are similar [25]. Lee and Vafai [30] stated that, for the case where the Biot number is high and the ratio of the fluid to the solid conductivity is very small, which is certainly the case for an aluminum foam air combination, the temperature difference between the solid and the fluid is nearly uniform over the foam cross section, and the temperatures of the solid and the fluid have approximately the same value.

3.1. *Grid sensitivity analysis*

In order to determine at what number of element the solution of the governing partial differential equations (PDEs) becomes grid independent. A grid independence study was conducted on the finite element mesh. The COMSOL mesh uses triangular elements with local triangular element refinement. The solution for steady flow through the metallic foam has been performed at different number of domain elements. The metallic foam model was solved five different times. The number of elements used to create the mesh (500 elements, 1030 elements, 1630 elements, 3130 elements, and 6606 elements) was adopted in order to determine the most efficient mesh size (in terms of change in resulting temperatures vs. computation time).

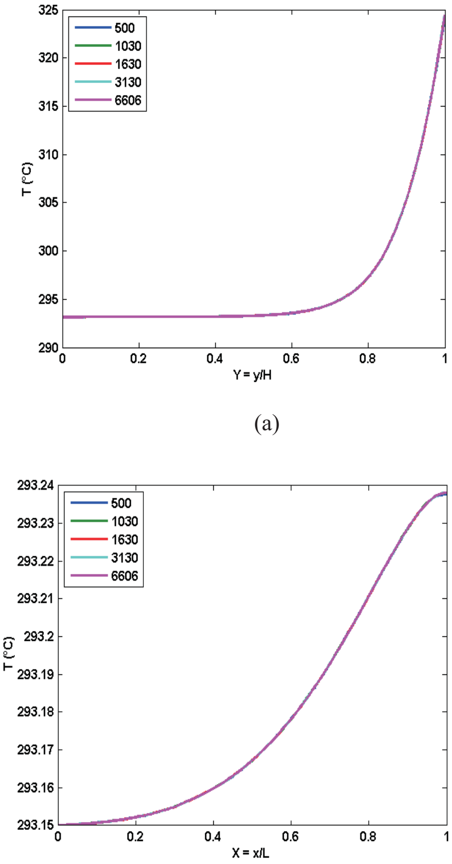

(a)

(b)

Figure 2 Grid Sensitivity Analysis: a) the temperature versus the none-dimensional axe Y = y/H, b) the temperature versus the none-dimensional axe X = x/L

Fig. 2 shows the temperature profiles inside the metallic foam versus the dimensionless axes Y and X respectively. The solution reached constant with variation less than 1E-03 % at number of elements (N) = 6606 elements.

Fig. 3 shows the relative error of temperature versus the number of elements for four different mesh points ($\mathrm{T}|_{(x=L/3,\ y=H)}$, $\mathrm{T}|_{(x=2L/3,\ y=H)}$, $\mathrm{T}|_{(x=L/3,\ y=H/3)}$ and $\mathrm{T}|_{(x=2L/3,\ y=2H/3)}$). The decreasing profiles of the relative error take very small values which can be reach a value of 1E-04 % at the number of elements N = 6606. As seen in Tab. 1, a mesh size of 6606 elements was chosen as ideal as any greater number of elements which did not produce a significant change of resulting temperatures.

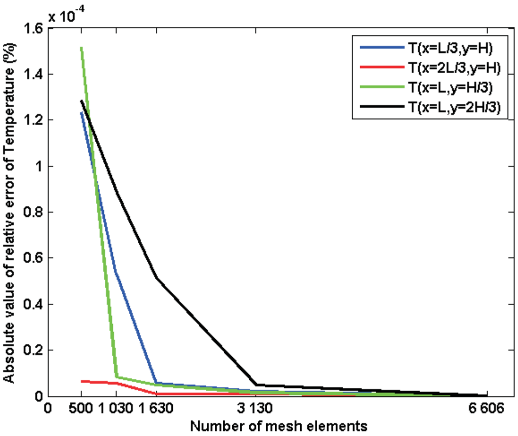

Figure 3 The diagram of grid independent test on absolute relative error of temperature

Table 2 Grid independent study

Number of mesh elements	Number of deg. of freedom solved	Comp. time (s)	$\mathrm{T}\|_{(x=L/3,\ y=H)}$ (K)	$\frac{\|\Delta T\|}{T}$ (%)	$\mathrm{T}\|_{(x=2L/3,\ y=2H/3)}$ (K)	$\frac{\|\Delta T\|}{T}$ (%)
500	3896	9	318.262567	1E-04	296.0773891	3E-04
1030	7635	11	318.262174	5E-05	296.0774903	4E-04
1630	11815	12	318.262342	5E-06	296.0705105	5E-05
3130	21894	16	318.262359	2E-06	296.0706622	4E-05
6606	45981	39	318.262365		296.0705191	

3.2. *CFD model validation*

The CFD model adopted in this study was validated with the experimental data of Dukhan and Chen [20] which are based on the direct temperature measurements inside the asymmetrically heated aluminum foams. Figs. 4 are plots of dimensionless temperature $Teta = (\mathrm{T} -\ \mathrm{T}_0)\, k_f/\mathrm{q}_\mathrm{W}\mathrm{H}$ versus the none-dimensional axe Y = y/H. The comparison between simulated temperature profiles and experimental data is given for the 10 ppi aluminum foam having a porosity of 68.6% at inlet velocity of 2.71 m/s, the 10 ppi aluminum foam having a porosity of 79.6% at inlet velocity of 2.50 m/s and the 20 ppi foam having a porosity of 78.2% at inlet velocity of 2.79 m/s, respectively.

The experimental data and the numerical predictions are given for the none-dimensional axial distances X = x/H = 0.125, 0.250 and 0.375, which correspond to the physical distances 1.27, 2.54 and 3.81 cm from the inlet of the foam block. The temperature increases as the distance to the heated base decreases, in a similar manner to an exponential growth. CFD temperature results and experimental data are in good agreement but there is a small discrepancy between them at specific locations. This may result from the uncertainties in the thermocouple's location, air velocity, temperature readings and heat flux [20].

3.3. *Heat transfer*

Fig. 5 illustrates the temperature distribution and the temperature contours inside the three types of aluminum foam: the 10 ppi foam with a porosity of $\varepsilon = 68.6\%$, the 20 ppi foam with a porosity of $\varepsilon = 78.2\%$ and the 40 ppi foam with a porosity of $\varepsilon = 93.5\%$. The foam is a rectangular block heated by its top surface with a constant and uniform heat flux $\mathrm{q}_w = 2.99$ (W/cm^2), and it is exposed to the air flow in the axial direction with a constant average velocity u_0= 2 m/s, and ambient temperature T_0 = 293.15 K. For the three types of foam, the hottest region is located at the top surface. As air acts as a coolant in the axial direction, this zone is located at the right corner of the block. Maximum temperatures in the corresponding zone are 308.92 K for the 10 ppi foam, 313.74 K for the 20 ppi foam, and 337.02 K for the 40 ppi foam, respectively.

Fig. 6 shows a comparison of the temperature profiles at different locations (x = L/4, x = L/2, and x = L) of the transverse direction within the aluminum foams. The 40 ppi aluminum foam shows a larger temperatures, followed by the 20 ppi, and then by the 10 ppi. The increasing of the foam porosity, increases the metal content of the foam, and thus allowing more heat conduction form the heated face into and through the foam in the transverse direction, and causing the higher temperatures.

3.4. *Velocity*

The dimensionless velocity profile inside the three types of aluminum foam 10-, 20-, 40- pore per inch at the dimensionless axial location X = 0.5 is presented in Fig. 7. It is shown that dimensionless velocity of air can be assumed to be constant across the height of the foam block, except near the top and the bottom walls where there is a step velocity gradient due to no-slip boundary condition. This result coincides with the results of many authors [36, 37].

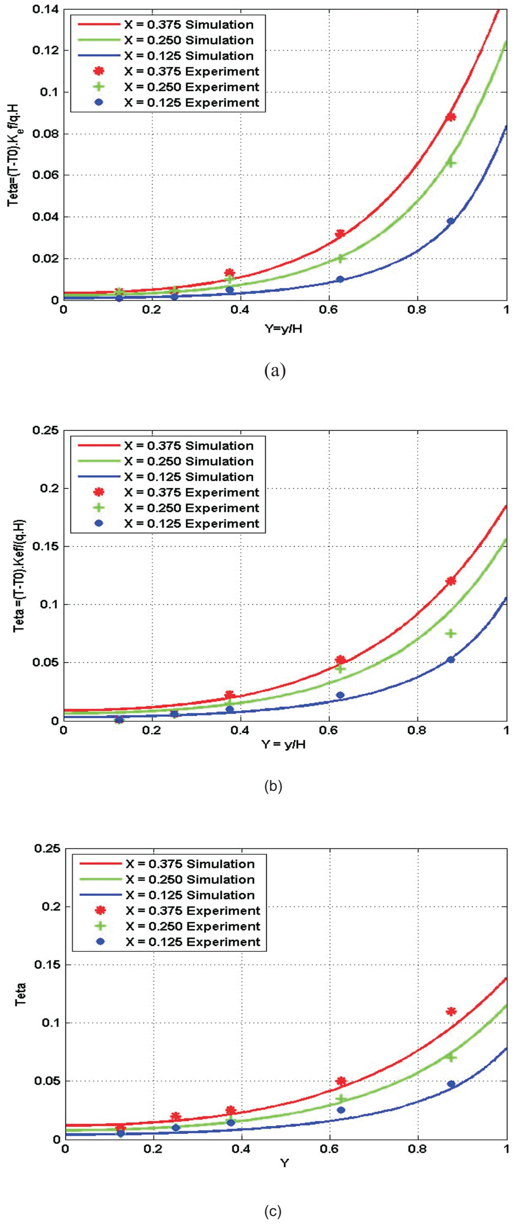

(a)

(b)

(c)

Figure 4 Comparison of the present CFD results with the experimental ones for the three types of foam: (a) 10 ppi, 68.6% aluminum foam, (b) 10 ppi, 79.6% aluminum foam and (c) 20 ppi, 78.2% aluminum foam

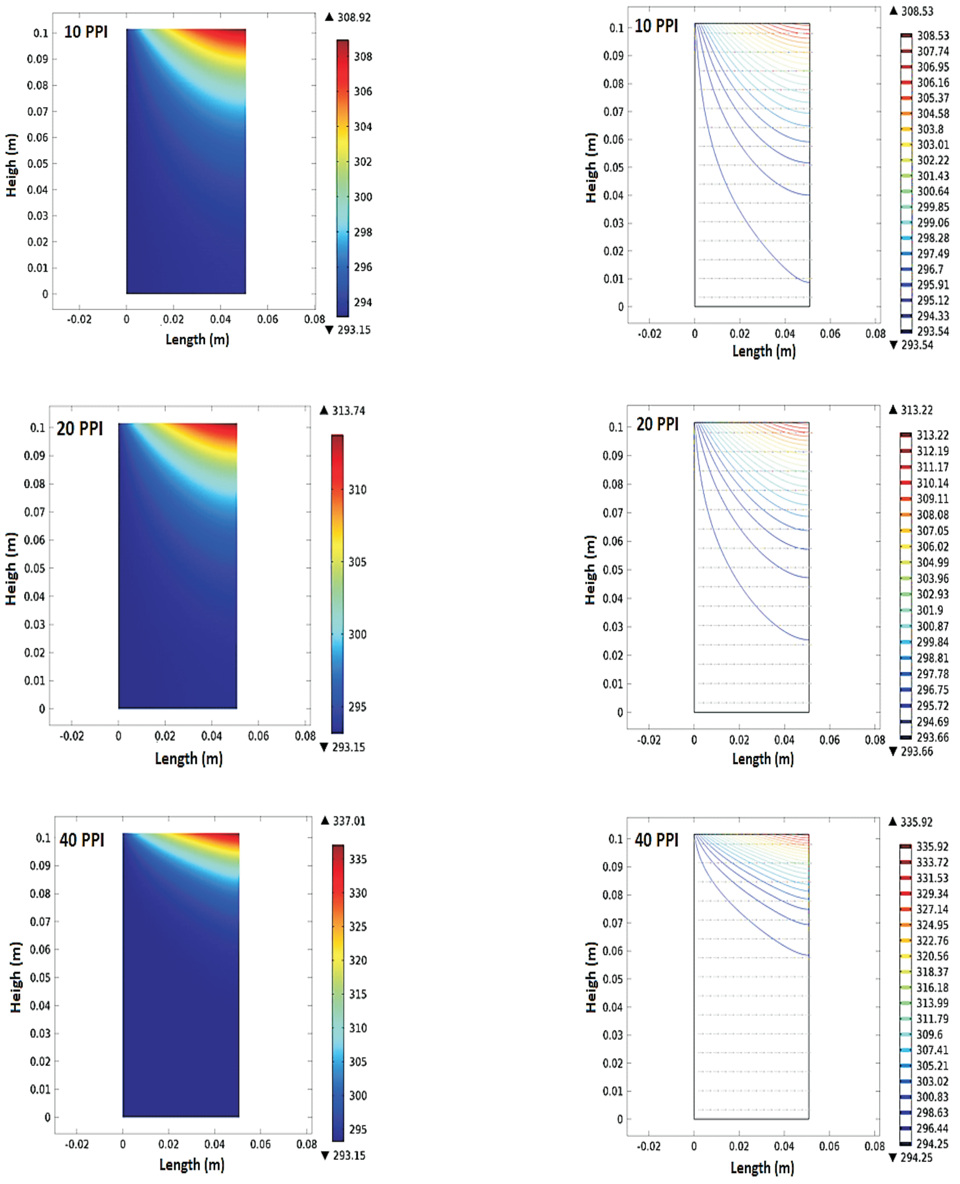

Figure 5 Temperature distribution and temperature contours inside the three types of aluminum foam: 10 ppi foam with a porosity of ε = 68.6%, 20 ppi foam with a porosity of ε = 78.2% and 40 ppi foam with a porosity of ε = 3.5% in conditions of $q_w = 2.99$ (W/cm^2) and $u_0 = 2$ m/s

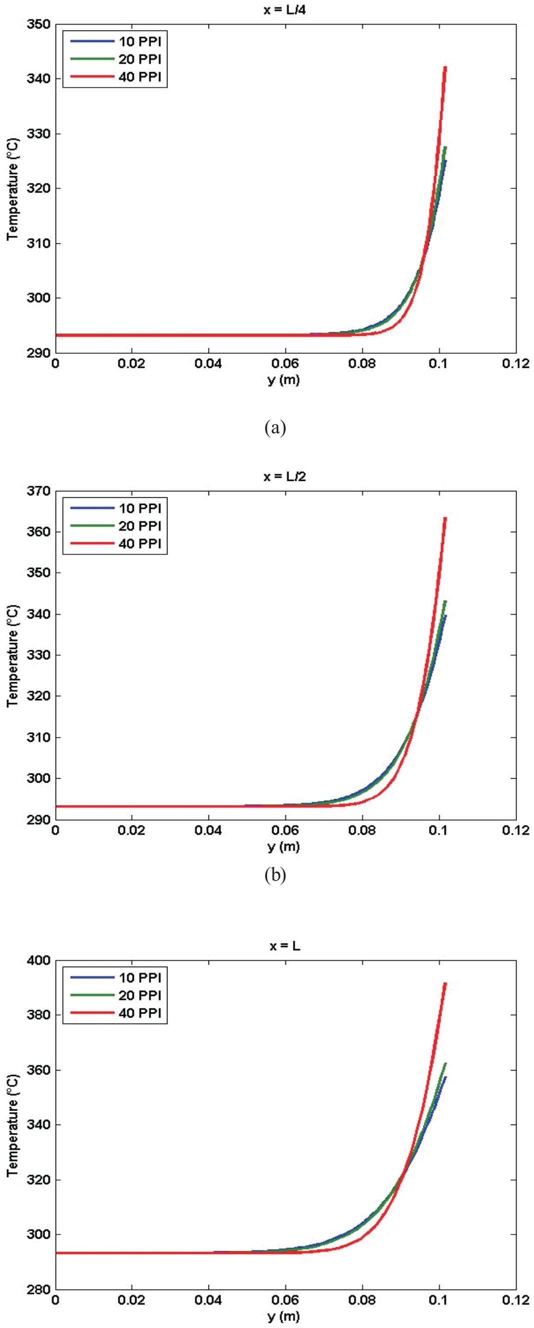

(a)

(b)

(c)

Figure 6 Comparison of temperature profiles for the three types of aluminum foam (10 ppi, 20 ppi and 40 ppi) at different locations: a) x = L/4, b) x = L/2 and c) x = L, in conditions of q_w=2.99 (W/cm^2) and u_0= 2 m/s

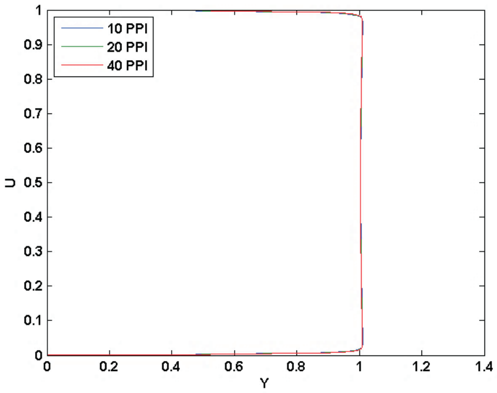

Figure 7 Dimensionless velocity at X = 0.5 inside the aluminum foams for q_w=2.99 W/cm^2 and u_0 =2m/s

This behavior is due to the strong flow-mixing capability of the open-cell porous structures. The dimensionless velocity profile remains unchanged along the flow direction of the fluid inside the three types of aluminum foam. As a result, the fluid flow can be modeled as plug flow [38].

3.5. *Pressure drop*

The dimensionless pressure profile inside the three types of aluminum foam 10-, 20-, 40- pore per inch, at the dimensionless axial location Y = 0.5, in the conditions of q_w = 2.99 W/cm^2 and u_0 = 2 m/s is presented in Fig. 8. Dimensionless pressure decreases linearly along the flow direction. Consequently, pressure drop increases linearly inside the foams along the flow direction. This result coincides with the results of many authors [16, 35]. Pressure drop is almost identical for the three types of the aluminum foam. This is an expected behavior because of the very close values of the foams permeability.

3.6. *Reynolds number effect*

To study the effect of Reynolds number on the flow and temperature fields, calculations were carried out at Re = 250, 500, 1000, and 2000, respectively, for the three types of aluminum foam, with the imposed heat flux q = 0.8 W/cm^2. Temperature distribution presented in Figs. 9–11, and comparison of local temperature profiles T-Y variations in Fig. 12 inside the foam block at x = L/2, show that at higher Reynolds number, the local temperature becomes lower. The reason for this trend is that at larger Reynolds number, the more low temperature core fluid passes over heater porous matrix, This, in turn, increases significantly the heat transfer by convection within the foam. Due to the Reynolds number effect on the temperature field inside the porous medium, the foam with the largest number of pores presents extended heat transfer surfaces. The result is a larger temperature gradient; therefore the 40ppi foam shows a higher temperature gradient than those of 20 PPI and 10 PPI.

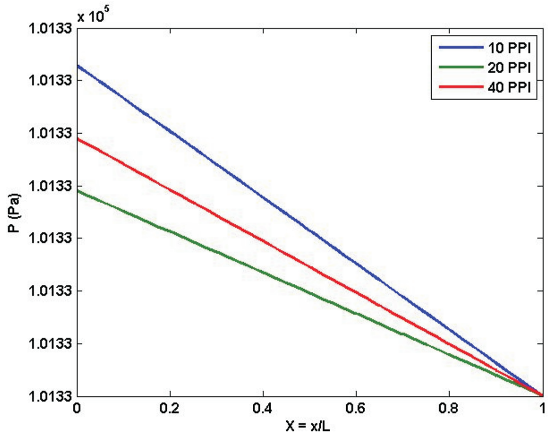

Figure 8 Pressure profiles inside the aluminum foams at Y $= 0.5$ for $q_w = 2.99$ W/cm^2 and u_0=2 m/s

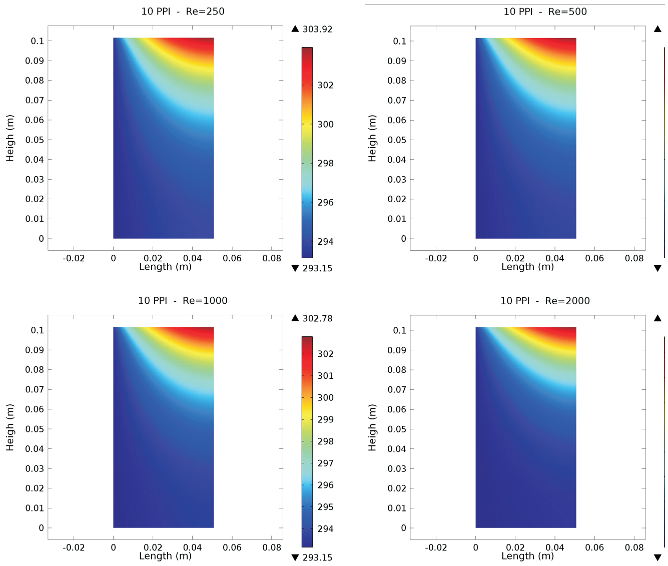

Figure 9 Temperature distribution inside the 10 ppi aluminum foam with a porosity of $\varepsilon = 68.6\%$ at different Reynolds number (250, 500, 1000 and 2000)

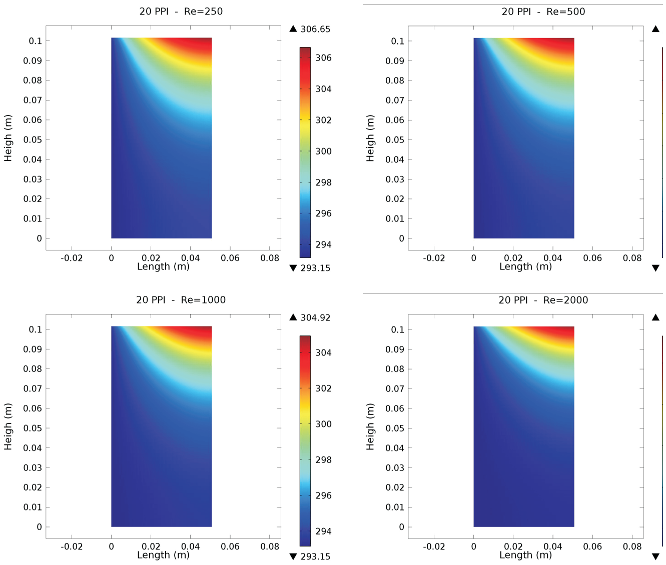

Figure 10 Temperature distribution inside the 20 ppi aluminum foam with a porosity of $\varepsilon = 78.2\%$ at different Reynolds number (250, 500, 1000 and 2000)

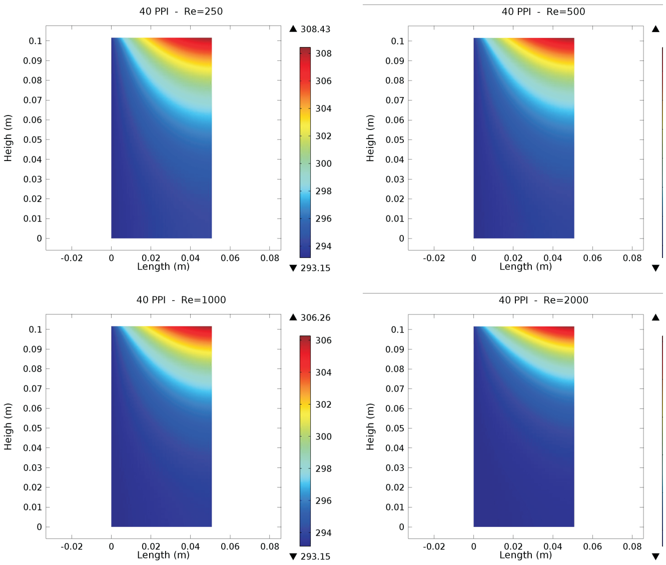

Figure 11 Temperature distribution inside the 40 ppi aluminum foam with a porosity of $\varepsilon = 93.5\%$ at different Reynolds number (250, 500, 1000 and 2000)

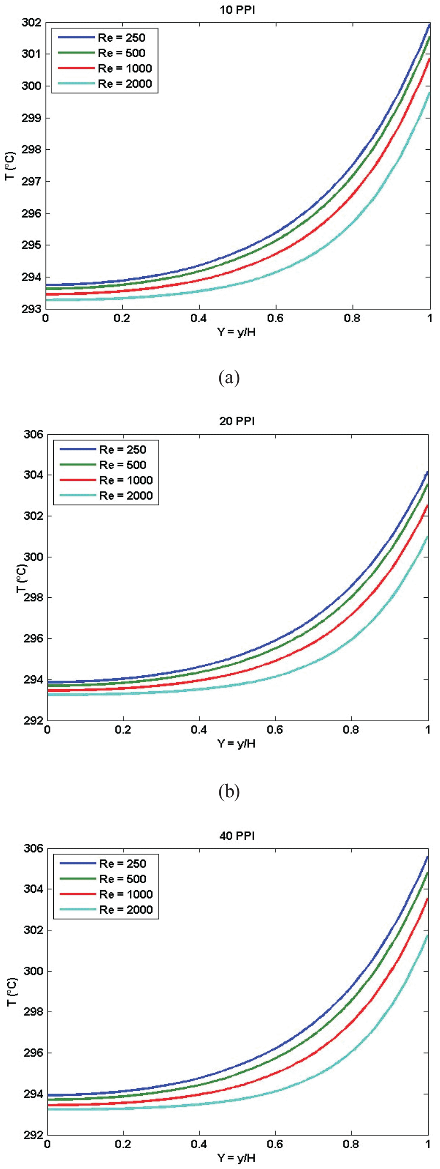

(a)

(b)

(C)

Figure 12 Comparison of local temperature profiles at x = L/2, with the imposed heat flux q = 0.8 W/cm^2, at different Reynolds number (250, 500, 1000 and 2000), inside the three types of foam: a) 10 ppi aluminum foam with a porosity of $\varepsilon = 68.6\%$, b) the 20 ppi aluminum foam with a porosity of $\varepsilon = 78.2\%$, and c) 40 ppi aluminum foam with a porosity of $\varepsilon = 93.5\%$

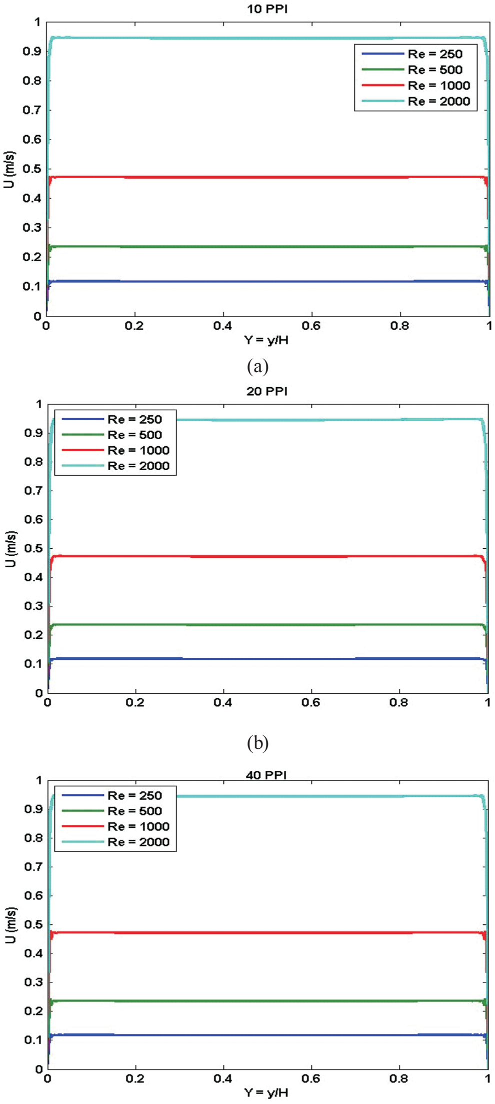

(a)

(b)

(c)

Figure 13 Comparison of the velocity profiles at x = L/2, with the imposed heat flux q = 0.8 W/cm^2, at different Reynolds number (250, 500, 1000 and 2000): a) 10 ppi aluminum foam with a porosity of $\varepsilon = 68.6\%$, b) the 20 ppi aluminum foam with a porosity of $\varepsilon = 78.2\%$, and c) 40 ppi aluminum foam with a porosity of $\varepsilon = 93.5\%$

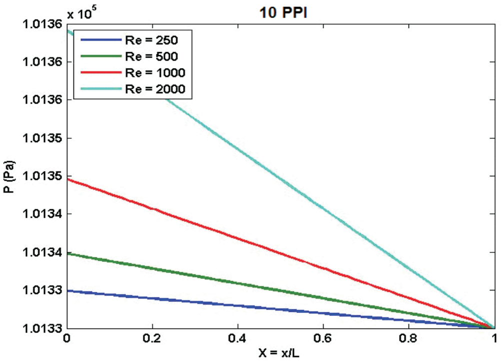

(a)

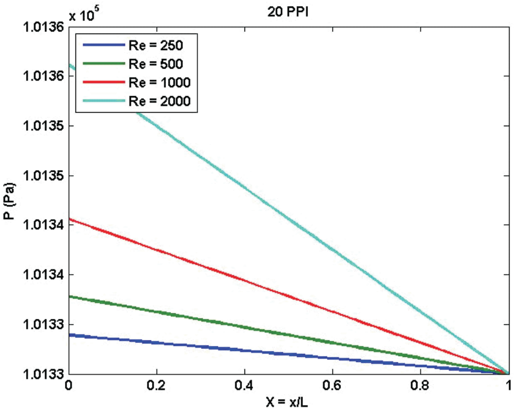

(b)

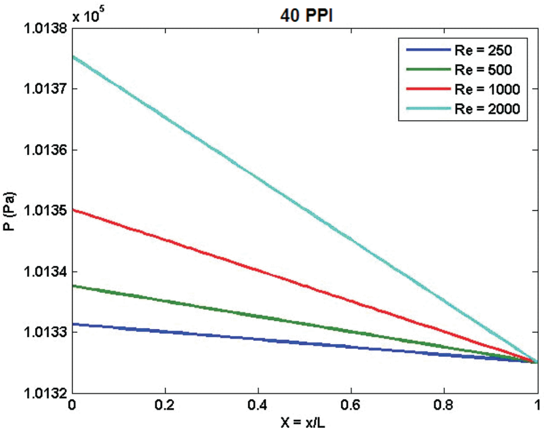

(c)

Figure 14 Comparison of the pressure profiles at y = H/2, with the imposed heat flux q = 0.8 W/cm^2, at different Reynolds number (250, 500, 1000 and 2000), inside the three types of foam: a) 10 ppi aluminum foam with a porosity of $\varepsilon = 68.6\%$, b) the 20 ppi aluminum foam with a porosity of $\varepsilon = 78.2\%$, and c) 40 ppi aluminum foam with a porosity of $\varepsilon = 93.5\%$

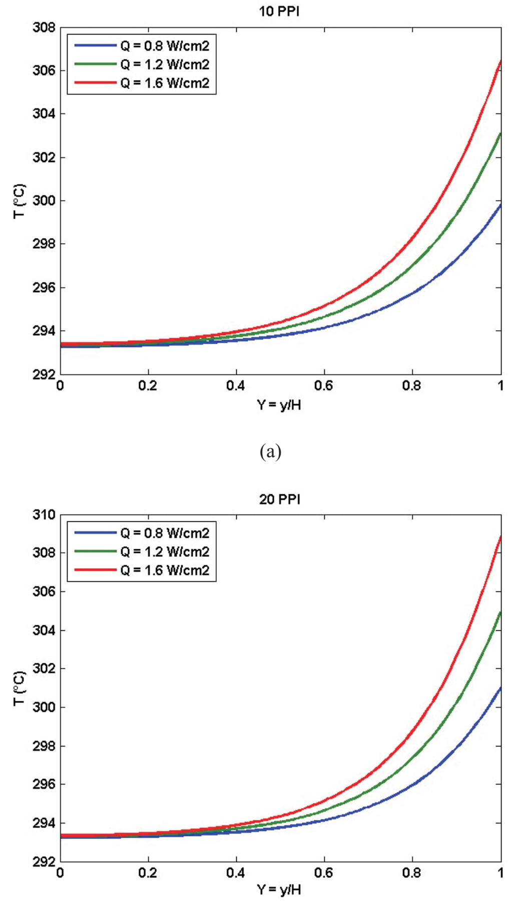

(a)

(b)

Figure 15 Comparison of the temperature profiles at x = L/2, with different imposed heat flux q = (0.8, 1.2, and 1.6) W/cm^2, inside the three types of foam: a) 10 ppi aluminum foam with a porosity of $\varepsilon = 68.6\%$, b) the 20 ppi aluminum foam with a porosity of $\varepsilon = 78.2\%$, and c) 40 ppi aluminum foam with a porosity of $\varepsilon = 93.5\%$

Comparison of the velocity profiles U-Y variations in Fig. 13, at different Reynolds number Re = 250, 500, 1000, and 2000, respectively, for the three types of foam, with the imposed heat flux q = 0.8 W/cm^2, shows that as Re increases, the internal structure of the porous media has a greater effect on velocity profiles, which becomes flatter. The strong flow-mixing inside the porous structures makes the hydrodynamic boundary layer thickness smaller. This result coincides with the result mentioned in the reference [16].

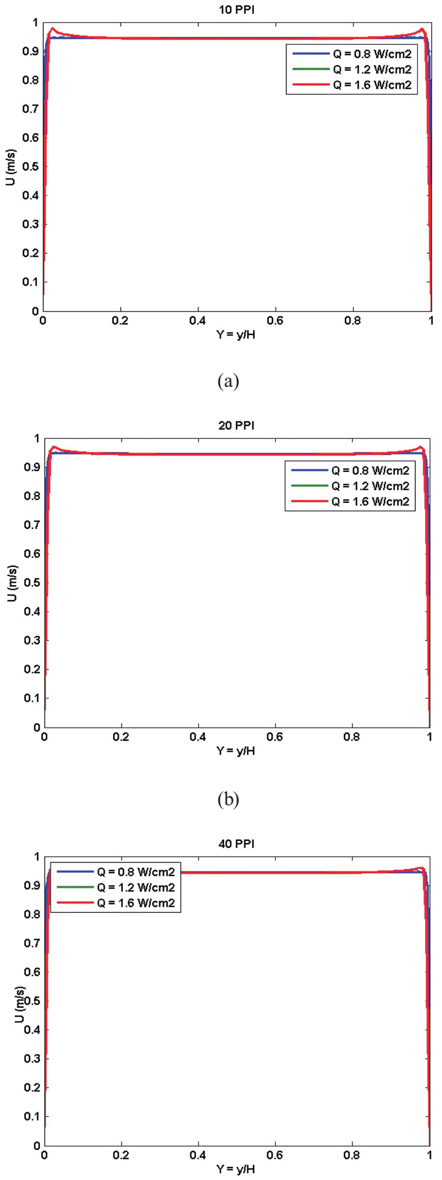

(a)

(b)

(c)

Figure 16 Comparison of the velocity profiles at y = H/2, with different imposed heat flux q = (0.8, 1.2, and 1.6) W/cm^2, inside the three types of foam: a) 10 ppi aluminum foam with a porosity of $\varepsilon = 68.6\%$, b) the 20 ppi aluminum foam with a porosity of $\varepsilon = 78.2\%$, and c) 40 ppi aluminum foam with a porosity of $\varepsilon = 93.5\%$

Fig. 14 shows a comparison of pressure profiles inside the three types of aluminum foam 10-, 20-, 40- pore per inch, at different Reynolds number (250, 500, 1000 and 2000), and at the transverse location y = H/2, with the imposed heat flux $q_w = 2.99$ W/cm^2. Pressure profiles decrease linearly along the flow direction. And thus, pressure drops increase linearly inside the foams along the flow direction. The foam with the largest density of pores presents extended surfaces (pores and ligaments) that exhibit a resistance to the air flow. The result is a larger pressure drop within the foam; therefore the 40 ppi foam shows a higher pressure drop than those of 20 ppi and 10 ppi.

3.7. *Heat flux effect*

The heat flux imposed on the upper face of the foam block showen in Fig. 15 promotes the propagation of the heat by conduction in the porous matrix, which increases the equilibrium temperature between the two phases of the foam solid and gaseous. The 40 ppi foam shows higher temperatures than those shown for the other foams. As the porosity increases, the metal content of the foam becomes larger allowing more heat conduction form the heated face into and through the foam in the transverse direction, and thus causing the higher temperatures.

The effect of the imposed heat flux on the flow shown in Fig. 16 is not appreciable. For a heat flux which varies from 0.8 to 1.6 W/cm^2, velocity profiles for the three types of foam are almost identical. For this range of heat flux variation, the effect of air comprehensibility within the foam does not appear, and the flow remains unchanged.

4. Conclusions

CFD modeling of heat transfer and fluid flow within aluminum foams subjected to constant heat flux on one side, and cooled by a confined air flow, was presented. A two energy equations heat transfer model for porous media was adopted from the literature. For fluid flow, the Brinkman-Forchheimer extended Darcy model is considered to predict the dynamic behavior of the fluid transfer to the interior of metallic foams. COMSOL multiphysics software is used to solve the governing equations. The effects of Reynolds number range Re = 250-2000 and the imposed heat flux $q_w = 0.8$-1.6 (W/cm^2) on the fluid flow hydrodynamic parameters, as well as on the porous medium thermal characteristics are examined for the three types of aluminum foam10-, 20-, 40- pore per inch.

The following conclusions may be mentioned:

1. The grid sensitivity analysis proves that the CFD model realized by COMSOL software uses the most efficient mesh size, which gives better and accurate results.
2. Under the conditions of a constant imposed heat flux, and a constant air velocity at the inlet, the hottest region is located at the right corner of the top surface. The level of temperature increases with increasing of the foam porosity.

3. Due to the strong flow-mixing capability of the foams structures. The velocity profile remains unchanged along the flow direction. As a result, the fluid flow can be modeled as plug flow over the range of parameter under consideration.

4. The pressure profile decreases linearly along the flow direction. Consequently, pressure drop increases linearly inside the foams. The 40 ppi foam shows a higher pressure drop than those of 20 ppi and 10 ppi.

5. The effect of Reynolds number on the temperature field is due mainly to the forced convection of air, a temperature gradient within the foam in the transverse of flow direction increases with increasing of the foam porosity. The pressure drop becomes larger under the condition of the forced convection.

6. The effect of the imposed heat flux on the temperature field is due mainly to the heat conduction inside the porous matrix, The increasing of the foam porosity, increases the metal content of the foam, and thus allowing more heat conduction form the heated face into and through the foam in the transverse direction, and causing the higher temperatures. The velocity and pressure drop rest unchanged under the envisaged conditions of imposed heat flux.

7. The CFD results generally showed qualitative agreement with experimental data from the literature.

8. In perspective for this work, the effect of the Reynolds number in transient and turbulent flow regimes must be examined.

Acknowledgements

This work was carried out in the Grenoble electrical engineering laboratory (G2ELab) in the Republic of France. The authors grateful acknowledge the support of this laboratory to accomplish this work.

References

[1] **Dai, Z., Nawaz, K., Park, Y., Chen, Q. and Jacobi, A. M.**: A comparison of metal–foam heat exchangers to compact multilouver designs for air-side heat transfer applications, *Heat Transfer Eng*, 33, 1, 21–30, **2012**.

[2] **Boyd, B. and Hooman, K.**: Air-cooled micro-porous heat exchangers for thermal management of fuel cells, *Int. Commun. Heat Mass Transfer*, 39, 363–367, **2012**.

[3] **Hutter, C., Büchi, D., Zuber, V. and von Rohr, R.**: Heat transfer in metal foams and designed porous media, *Chem. Eng. Sci*, 66, 3806–3814, **2011**.

[4] **Wu, Z., Caliot, C., Flamant, G. and Wang, Z.**: Numerical simulation of convective heat transfer between air flow and ceramic foams to optimise volumetric solar air receiver performances, *Int. J. Heat Mass Transfer*, 54, 1527–1537, **2011**.

[5] **Ji, X., Xu, J. and Abanda, A. M.**: Copper foam based vapor chamber for high heat flux dissipation, *Exp. Therm. Fluid Sci*, 40, 93–102, **2012**.

[6] **Wan, Z. M., Guo, G. Q., Su, K. L., Tu, Z. K. and Liu, W.**: Experimental analysis of flow and heat transfer in a miniature porous heat sink for high heat flux application, *Int. J. Heat Mass Transfer*, 55, 4437–4441, **2012**.

[7] **Zhao, C.Y.**: Review on thermal transport in high porosity cellular metal foams with open cells, *Int. J. Heat Mass Transfer*, 55, 3618–3632, **2012**.

[8] **Mancin, S., Zilio, C., Diani, A. and Rossetto, L.**: Air forced convection through metal foams: Experimental results and modeling, *Int. J. Heat Mass Transfer*, 62, 112–123, **2013**.

[9] **Bhattacharya, A., Calmidi, V. V. and Mahajan, R. L.**: Thermophysical Properties of High Porosity Metal Foams, *Int. J. Heat Mass Transfer*, 45, 1017-1031, **2002**.

[10] **Phanikumar, M. S. and Mahajan, R. L.** : Non-Darcy natural convection in high Porosity metal foams, *Int. J. Heat Mass Transfer*, 45, 3781–3793, **2002**.

[11] **Haji-Sheikh, A. and Vafai, K.**: Analysis of flow and heat transfer in porous media imbedded inside various-shaped ducts, *Int. J. Heat Mass Transfer*, 47, 1889–1905, **2004**.

[12] **Alvarez-Hernandez, A. R.**: *Combined Flow and Heat Transfer Characterization of Open Cell Aluminum Foams*, M.Sc. Thesis, University of Puerto Rico, **2005**.

[13] **Dukhan, N.**: Correlations for the pressure drop for flow through metal foam, *Exp. Fluids*, 41, 665–672, **2006**.

[14] **Minkowycz, W. J. and Haji-Sheikh, A.**: Heat transfer in parallel plates and circular porous passages with axial conduction, *Int. J. Heat Mass Transfer*, 49, 2381–2390, **2006**.

[15] **Kopanidis, A., Theodorakakos, A., Gavaises, E. and Bouris, D.**: 3D numerical simulation of flow and conjugate heat transfer through a pore scale model of high porosity open cell metal foam, *Int. J. Heat Mass Transfer*, 53, 2539–2550, **2010**.

[16] **Chen C., Huang P. and Hwang H.**: Enhanced forced convective cooling of heat sources by metal-foam porous layers, *Int. J. Heat Mass Transfer*, 58, 356–373, **2013**.

[17] **Bai, M. and Chung, J.N.**: Analytical and numerical prediction of heat transfer and pressure drop in open-cell metal foams, *Int. J. Thermal Sciences*, 50, 869–880, **2011**.

[18] **Dukhan, N. and Ali, M.**: Strong wall and transverse size effects on pressure drop of flow through open-cell metal foam, *Int. J. Thermal Sciences*, 57, 85–91, **2012**.

[19] **Ranut, P., Nobilea, E. and Mancini L.**: High resolution microtomography-based CFD simulation of flow and heat transfer in aluminum metal foams, *Applied Thermal Engineering*, XXX, 1–11, **2013**.

[20] **Dukhan, N. and Chen, K.**: Heat transfer measurements in metal foam subjected to constant heat flux, *Experimental Thermal and Fluid Science*, 32, 624–631, **2007**.

[21] **Bhattacharya, A., Calmidi, V. V. and Mahajan, R. L.**: Thermophysical properties of high porosity metal foams, *Int. J. Heat Mass Transfer*, 45, 1017–1031, **2002**.

[22] **Calmidi, V. V.**: *Transport phenomena in high porosity metal foams*, PhD. Thesis, University of Colorado Boulder CO **1998**.

[23] **Calmidi, V. V. and Mahajan, R. L.**: The effective thermal conductivity of high porosity metal foams, *ASME J. Heat Transfer,* 121, 466–471, **1999**.

[24] **Koch, D. L. and Brady, J. F.**: The effective diffusivity of fibrous media, *AIChE J.,* 32, 575–591, **1986**.

[25] **Calmidi, V. V. and Mahajan, R. L.**: Forced convection in high porosity metal foams, *ASME J. Heat Transfer*, 122, 557–565, **2000**.

[26] **Zhukauskas, A.**: Heat Transfer from Tubes in Cross Flow, *Advances in Heat Transfer, Academic Press*, New York, vol. 8, **1972**.

[27] **Thomas, E. and Karan, K.**: Methodology for determining volumetric convection coefficients in metallic foam monoliths coated with ceramic catalyst support, *Thermal Issues in Emerging Technologies, ThETA 2*, Cairo, Egypt, **2008**.

[28] **Calmidi, V. V. and Mahajan R. L.**: The effective thermal conductivity of high porosity metal foams, *ASME J. Heat Transfer*, 121, 466–471, **1999**.

[29] **Koch, D. L. and Brady, J. F.**: The effective diffusivity of fibrous media, *AIChE J.*, 32, 575–591, **1986**.

[30] **Lee, D. Y. and Vafai, K.**: Analytical characterization and conceptual assessment of solid and fluid temperature differentials in porous media, *International Journal of Heat and Mass Transfer*, 42, 423–435, **1999**.

[31] **Kim, S. J. and Jang, S. P.**: Effects of the Darcy number, the Prandtl number and the Reynolds number on the local thermal non-equilibrium, *International Journal of Heat and Mass Transfer*, 45, 3885–3896, **2002**.

[32] **Sullines, D. and Daryabeige, K.**: Effective thermal conductivity of high porosity open cell nickel foam, *35th AIAA Thermophysics Conference*, Anaheim CA, 2819, 12, **2001**.

[33] **Kim, S. J. and Kim, D.**: Forced convection in microstructures for electronic equipment cooling, *Journal of Heat Transfer,* 121, 639–645, **1999**.

[34] **Minkowycz, W. J., Haji-Sheikh, A. and Vafai, K.**: On departure from local thermal equilibrium in porous media due to a rapidly changing heat source: the Sparrow number, *International Journal of Heat and Mass Transfer*, 42, 3373–3385, **1999**.

[35] **Dukhan,N. and Carel, A. M.**: A two-permeability approach for assessing flow properties in metal foam, *Journal of Porous Mater,* 8, 417–424, **2011**.

[36] **Xu, H., Gong, L., Huang, S. and Xu, M.**: Non-equilibrium heat transfer in metal-foam solar collector with no-slip boundary condition, *Int. J. Heat Mass Transf*, 76, 357–365, **2014**.

[37] **Feng, S. S., Kuang, J. J., Wen, T., Lu, T. J. and Ichimiya K.**: An experimental and numerical study of finned metal foam heat sinks under impinging air jet cooling, *Int. J. Heat Mass Transf*, 77, 1063–1074, **2014**.

[38] **Solmus, I.**: Numerical investigation of heat transfer and fluid flow behaviors of a block type graphite foam heat sink inserted in a rectangular channel, *Applied Thermal Engineering*, 78, 605–615, **2015**.

[39] **Angirasa, D.**: Experimental investigation of forced convection heat transfer augmentation with metallic fibrous materials, *Int. J. Heat Mass Transf*, 45, 919–922, **2002**.

[40] http://rsta.royalsocietypublishing.org/content/368/1917/1999.

Nomenclature

C_F – friction coefficient (dimensionless)
C_p – heat capacity of fluid
d_f – fiber diameter
d_p – pore diameter
G – shape function
H – height of foam block
h_{sf} – convection heat transfer coefficient
K – permeability of the porous medium
k – thermal conductivity
L – length of foam block
N – number of mesh elements
Nu_x – local Nusselt number

p – pressure
p_0 – atmospheric pressure
Pr – Prandtl number (dimensionless)
ppi – number of pores per inch
Re – Reynolds number (dimensionless)
q_w – specific heat flux
T – temperature
$T_{w,x}$ – local wall temperature
T_0 – temperature entering foam
Teta – dimensionless temperature
U – dimensionless velocity in the x-direction
u – velocity component in the x-direction
u_D – Darcian velocity
u_0 – average velocity entering foam
v – velocity component in the y-direction
V – velocity vector
W – width of foam sample
X, Y – dimensionless Cartesian coordinates
x, y – Cartesian coordinates

Greek symbols

ε – porosity
ρ – density
α – specific surface area
Δ – change
μ – dynamic viscosity
ν – kinematic viscosity
σ – surface area per unit volume of foam

Subscripts

d – thermal dispersion
f – fluid
fe – fluid effective
$_0$ – inlet
s – solid
se – solid effective
w – wall